



# Facile synthesis of highly dispersed Ir/LaFeO<sub>3</sub> catalysts for propene total oxidation

Feng Pan<sup>a</sup>, Weidong Zhang<sup>a,b,\*</sup>, Corinne Ferronato<sup>a</sup>, José Luis Valverde<sup>c</sup>, Anne Giroir-Fendler<sup>a,\*\*</sup>

<sup>a</sup> Université Claude Bernard Lyon 1, IRCELYON, UMR 5256 CNRS 43 boulevard du 11 novembre 1918, Villeurbanne 69622, France

<sup>b</sup> School of Chemistry and Chemical Engineering, Anhui Province Key Laboratory of Coal Clean Conversion and High Valued Utilization, Anhui University of Technology, Ma'anshan 243002, China

<sup>c</sup> Department of Chemical Engineering, Faculty of Chemical Science and Technology, University of Castilla-La Mancha, Avenida Camilo José Cela 12, 13005 Ciudad Real, Spain

## ARTICLE INFO

### Keywords:

Iridium supported catalyst  
LaFeO<sub>3</sub> perovskite  
VOCs  
Propene oxidation

## ABSTRACT

A series of Ir/LaFeO<sub>3</sub> catalysts calcined at 300–600 °C were synthesized by a solvent-free method and tested for propene total oxidation. Various characterizations depicted that iridium was well-dispersed on LaFeO<sub>3</sub> with no detectable iridium-related particles or aggregates. The loading of iridium hardly changed the structural and textural properties of LaFeO<sub>3</sub>, but greatly enhanced the low-temperature reducibility and oxygen mobility, leading to superior propene oxidation activity. For Ir/LaFeO<sub>3</sub> series, the catalytic activity decreased as the calcination temperature increased, due to the declined reducibility and active oxygen species content. Ir/LaFeO<sub>3</sub>-300 was demonstrated to be the optimal catalyst with the best propene oxidation performance (T<sub>90</sub> = 246 °C), excellent long-term stability, and decent water-resistance. Treating Ir/LaFeO<sub>3</sub>-300 in a reducing atmosphere further improved its catalytic performance by enhancing low-temperature reducibility and increasing surface-active oxygen species. Overall, this study provides insights into the synthesis of highly efficient and stable iridium-based catalysts for VOCs oxidation.

## 1. Introduction

Volatile organic compounds (VOCs) have been recognized as one of the major air pollutants, which are responsible for the formation of tropospheric ozone, photochemical smog and secondary organic aerosols [1–3]. Due to their detrimental impact on the environment, several technologies have been developed to control and eliminate VOCs, of which catalytic oxidation has been extensively studied because of its higher efficiency and lower energy consumption [4,5]. Generally, two types of catalysts are applied for VOCs degradation, including supported noble metal catalysts and metal oxide catalysts [6]. It is well-known that noble metal catalysts exhibit superior catalytic activity than metal oxide catalysts for the degradation of most VOCs. Nevertheless, the scarcity and high cost of noble metals, such as Pt, Pd, and Rh, pose challenges to sustainable industrial processes. [7–9]. Consequently, there is a growing interest in enhancing the catalytic performance while reducing noble metal loadings.

Nowadays, catalysts based on Pt and Pd have become the primary catalysts in the industry and have been extensively used for the catalytic oxidation of VOCs [10–14]. Tahsini et al. [15] reported that Pt-Cu alloy presented a superior catalytic activity for propene oxidation. Wang et al. [16] found that the TiO<sub>2</sub> nanosheet-supported Pt nanocatalysts exhibited good stability and water resistance for the catalytic removal of a toluene and acetone mixture. In addition, an intelligent Pd/perovskite catalyst with a self-regenerative function was developed by Tanaka et al. [17] for automotive emission control. Ri et al. [18] prepared supported Pd catalysts for toluene oxidation, which exhibited excellent catalytic performance as well as good reusability, stability and water resistance. Despite being a member of the Pt group metals with comparable activity, less attention has been paid to supported iridium (Ir) catalysts for the total oxidation of VOCs [19]. Schick et al. [19,20] conducted a thorough investigation into the effects of Ir particle size and support on the catalytic oxidation of VOCs over supported Ir catalysts. Their results indicated that the small particle size of iridium favors the oxidation of

\* Corresponding author at: Université Claude Bernard Lyon 1, IRCELYON, UMR 5256 CNRS 43 boulevard du 11 novembre 1918, Villeurbanne 69622, France.

\*\* Corresponding author.

E-mail addresses: [weidong.zhang@ahut.edu.cn](mailto:weidong.zhang@ahut.edu.cn) (W. Zhang), [anne.giroir-fendler@ircelyon.univ-lyon1.fr](mailto:anne.giroir-fendler@ircelyon.univ-lyon1.fr) (A. Giroir-Fendler).

short-chain alkanes, the nature and acidity of the support also played a critical role. Li et al. [21] achieved complete oxidation of HCHO at ambient temperature on an Ir/Al<sub>2</sub>O<sub>3</sub> catalyst, with Ir<sup>0</sup> species being the active sites. Li et al. [22] demonstrated that Na addition had a dramatic promotion effect on Ir-based catalysts for ambient HCHO oxidation.

Due to their high surface energy and mobility, noble metal particles tend to aggregate during the calcination process. To maximize the utilization of noble metals and achieve high catalytic activity, it is crucial to prepare supported noble metal catalysts with high dispersion [23,24]. Dan et al. [25] obtained a high-dispersed core-shell structure Au@SiO<sub>2</sub> catalyst by preparation of Au colloids with tetradecyltrimethylammonium bromide, which significantly enhanced the catalytic performance for HCHO oxidation. Similarly, Gu et al. [26] reported the synthesis of atomically dispersed Pt on WO<sub>3</sub> using a colloidal template method with ethylene glycol and methanol as solvents, which greatly increased the active sites, thus leading to highly efficient oxidation of triethylamine. Chen et al. [27] synthesized Pt/Al<sub>2</sub>O<sub>3</sub> catalysts by a modified ethylene glycol reduction approach and found that higher dispersion of Pt led to the increase of adsorbed oxygen content and the promotion of benzene degradation efficiency. Liu et al. [28] prepared Ir/TiO<sub>2</sub> by a deposition-precipitation process using urea as the precipitator, the result indicates that the high dispersion of iridium on the Ir/TiO<sub>2</sub> catalyst facilitates the decomposition of N<sub>2</sub>O.

It is worth noting that the synthesis of highly dispersed supported noble metal catalysts commonly requires the utilization of excessive organic solvents, which could cause environmental pollution. In addition, the evaporation of the solvent is a time-consuming process. Therefore, it is desirable to develop a solvent-free strategy that can achieve high dispersion of noble metal. Recently, Liu et al. [29] adopted a simple and scalable approach to preparing thermally stable single-atomic Ru catalysts by physical mixing of bulk RuO<sub>2</sub> with spinel support and subsequent annealing, which could be extended to Ir-supported catalysts. La-based perovskite oxides with superior thermally stable structures are ideal supports for noble metals. It has been reported that the strong metal support interaction between Fe and Pt group metals is critical to the dispersion process [29]. LaFeO<sub>3</sub> was therefore chosen as the support for the synthesis of Ir catalysts. Propene is a representative VOC commonly presented in the chemical industry, motor vehicles, and aircraft exhausts, which is recognized as one of the most harmful environmental pollutants owing to its high photochemical ozone creation potential [30]. To the best of our knowledge, there are few references on propene oxidation over iridium-supported catalysts. Herein, high-dispersion iridium catalysts supported on LaFeO<sub>3</sub> were synthesized for the total oxidation of propene using an environmentally friendly solvent-free method. The influence of the calcination temperatures (300–600 °C) on the physicochemical properties and catalytic performance of Ir catalysts was thoroughly studied. The effect of water vapor and reduction treatment on the catalytic performance of the typical catalyst was also investigated.

## 2. Material and method

### 2.1. Synthesis

Firstly, LaFeO<sub>3</sub> was synthesized via a traditional citric acid method. 7 mmol La(NO<sub>3</sub>)<sub>3</sub> and 7 mmol Fe(NO<sub>3</sub>)<sub>3</sub> were dissolved in 50 mL distilled water at room temperature, followed by adding 16.8 mmol citric acid. The light-yellow solution was stirred at 80 °C to evaporate water. After foaming in the oven at 150 °C for 10 h, the sponge-like solid was ground and further calcined at 350 °C for 1 h and 650 °C for 8 h at a rate of 5 °C min<sup>-1</sup>.

Ir/LaFeO<sub>3</sub> was synthesized by a facile solvent-free method. Iridium acetylacetonate (Ir(acac)<sub>3</sub>) was employed as the iridium precursor. Ir(acac)<sub>3</sub> and LaFeO<sub>3</sub> were mixed and ground in a mortar for 10 min. The mixed powders were calcined at different temperatures (300–600 °C) for 5 h at the rate of 2 °C min<sup>-1</sup>. The obtained catalysts were named Ir/

LaFeO<sub>3-x</sub> (x = 300, 400, 500, 600). For comparison, commercial SiO<sub>2</sub>, TiO<sub>2</sub>, and Al<sub>2</sub>O<sub>3</sub> were also used as support for Ir catalysts by the same method and calcined at 300 °C for 5 h.

### 2.2. Characterization

The decomposition of Ir(acac)<sub>3</sub> and the mixture of Ir(acac)<sub>3</sub> and LaFeO<sub>3</sub> were analyzed by thermogravimetric and differential thermal analysis (TG-DTA) using a TGA/DSC1 STAR System Mettler Toledo from 25 °C to 950 °C in air-flow in alumina crucibles.

Iridium loading was measured by inductively coupled plasma-optical emission spectroscopy (ICP-OES, Horiba Jobin Yvon). Prior to the measurement, the samples were completely dissolved in H<sub>2</sub>SO<sub>4</sub> and aqua regia by heating at 250 °C.

The crystal information of samples was analyzed by X-ray diffraction (XRD) using Bruker D8 advance A25 diffractometer equipped with a Cu Kα radiation (λ = 0.154184 nm) at 40 kV × 40 mA. All the spectra were recorded from 10° < 2θ < 80° with a step size of 0.02° and a counting time of 2 s per step.

The Fourier transform infrared (FTIR) spectra were collected by a PerkinElmer FT-IR C92712 spectrometer from 400 to 4000 cm<sup>-1</sup> in attenuated total reflectance (ATR) mode with an instrument resolution of 2 cm<sup>-1</sup>. For every measurement, two spectra were accumulated.

Raman spectra were obtained by a LabRam HR Evolution (Horiba Scientific) spectrometer in the range of 50–1600 cm<sup>-1</sup> with a 532 nm Ar ion laser equipped with a CCD detector. The measurements were carried out under the microscope with a × 50 objective and 1 mW power.

Specific surface area (SSA) was determined by nitrogen adsorption-desorption isotherms using Micromeritics TRISTAR II apparatus at 77 K. Before the analysis, samples were degassed at 350 °C for 3 h under vacuum conditions. Barrett-Joyner-Halenda (BJH) method was chosen to calculate the total pore volume (V<sub>p</sub>).

High-resolution images of the solid were obtained by transmission electron microscopy using an FEI TITAN ETEM G2 microscope, operating at 300 KV and equipped with an objective Cs aberration corrector. In parallel, an energy-dispersive X-ray (EDX) analyzer (SDD X-Max 80 mm<sup>2</sup> from Oxford Instruments TM) was used to acquire the EDX spectra. For sample preparation, the powder was crushed and sonicated in ethanol, dropped onto a TEM grid, and dried by a lamp. To avoid contamination during analysis and remove all residual carbon, the samples were Ar-O<sub>2</sub> plasma-cleaned for 20 s.

X-ray photoelectron spectroscopy (XPS) measurement of the catalysts was performed on a Thermo Fisher ESCALAB 250Xi electron spectrometer with the excitation source of Al Kα (hν = 1486.6 eV) radiation. The charge of energy shift of the XPS spectra was corrected by setting the binding energy (B.E.) of contaminative carbon (C 1 s) at 284.6 eV. Analysis of the peaks was performed using the XPSPEAK41 software.

Temperature-programmed reduction with hydrogen (H<sub>2</sub>-TPR) experiments were conducted on a Thermo Scientific TPD/R/O 1110 Catalytic Surfaces Analyzer. The sample was first pretreated at 350 °C for 1 h in 5 % O<sub>2</sub>/He. After cooling down, it was reduced by 5 % H<sub>2</sub>/Ar from 50° to 950°C at a rate of 10 °C min<sup>-1</sup>.

### 2.3. Catalytic tests

The propene oxidation performance of the catalysts was examined using 0.1 g of the catalyst diluted with 0.5 g of SiC. The catalyst was sieved to a grain size of ~ 315 μm and loaded into a U-shape quartz tube reactor with an inner diameter of 4 mm. The feed gas was composed of 1000 ppm of propene and 21 vol% oxygen balanced with He. The total flow rate was controlled at 100 mL min<sup>-1</sup>, resulting in a weight hourly space velocity (WHSV) of 60000 mL h<sup>-1</sup> g<sub>cat</sub><sup>-1</sup>. The catalytic test was operated by a stabilizing-heating-aging and cooling process. The light-off curves were collected during the cooling ramp at a rate of 2 °C min<sup>-1</sup>.

Propene, CO, and CO<sub>2</sub> were detected by a gas chromatograph (SRA %

GC-R3000) coupled with a thermal conductivity detector. The temperature was measured by a thermocouple placed close to the middle of the catalytic bed.

Propene conversion (X) was calculated by the formula:

$$X = \frac{[\text{CO}_2]_{\text{outlet}}}{3[\text{C}_3\text{H}_6]_{\text{inlet}}} \cdot 100\%$$

where  $[\text{CO}_2]_{\text{outlet}}$  and  $[\text{C}_3\text{H}_6]_{\text{inlet}}$  refer to the concentrations of outlet  $\text{CO}_2$  and inlet  $\text{C}_3\text{H}_6$ , respectively.

Considering iridium as the active site, the specific reaction rate ( $r$ ,  $\text{s}^{-1}$ ) was calculated by the formula:

$$r = \frac{F \cdot X}{n_{\text{Ir}}}$$

where F is the molar flow rate ( $\text{mol s}^{-1}$ ), X is the propene conversion ( $X < 15\%$ ), and  $n_{\text{Ir}}$  is the molar quantity of iridium in the catalyst ( $\text{mol}$ ).

For the long-term durability test, the reaction temperature was maintained at  $230^\circ\text{C}$  for 35 h. The water influence was checked by introducing 5 vol%  $\text{H}_2\text{O}$  into the system, which was generated by bubbling in a water container immersed in a bath maintained at  $34^\circ\text{C}$ .

Propene oxidation without oxygen experiments were conducted on the same setup. 0.1 g of catalyst mixed with 0.5 g of SiC was first pretreated at  $300^\circ\text{C}$  for 0.5 h in helium to remove the impurities adsorbed on the surface of the sample. Once the temperature cooled down to  $50^\circ\text{C}$ , 1000 ppm of  $\text{C}_3\text{H}_6/\text{He}$  was introduced into the reactor. Finally, the temperature was raised to  $450^\circ\text{C}$  at the rate of  $5^\circ\text{C min}^{-1}$ , maintained for 2 h and then cooled down to room temperature. The amount of active oxygen species was calculated by the formula:

$$O_{\text{amount}} = \frac{3F_0AP_0 \cdot 10^{-6}}{RT_m}$$

where A is  $\text{CO}_2$  production ( $\text{ppm} \cdot \text{min}$ ),  $F_0$  is the volumetric flow rate ( $\text{m}^3 \text{min}^{-1}$ ), m is the mass of the catalyst (g),  $P_0$  is the atmospheric pressure ( $P_a$ ), R is the gas constant, T is room temperature (K) [31].

## 2.4. Reduction treatment

Reduction treatment was further performed on Ir/LaFeO<sub>3</sub>-300. The catalyst was pretreated at  $300^\circ\text{C}$  for 1 h in 10 %  $\text{H}_2/\text{He}$  or 1000 ppm  $\text{C}_3\text{H}_6/\text{He}$ . The reduced catalysts were fully characterized. Likewise, their catalytic activity and water resistance were examined under the same conditions as described in the catalytic tests part. For the long-term durability test, the reaction temperature was maintained at  $220^\circ\text{C}$  for 60 h.

## 3. Results and discussion

### 3.1. Structural property

To investigate the decomposition process of iridium precursor, TG/DTA was performed in an air stream. TG curves of  $\text{Ir}(\text{acac})_3$  and the mixture of  $\text{Ir}(\text{acac})_3$  and  $\text{LaFeO}_3$  were presented in Fig. S1. The  $\text{Ir}(\text{acac})_3$  remained stable when the temperature was below  $200^\circ\text{C}$ , followed by a fast weight loss (around 90 %) which ended at around  $330^\circ\text{C}$ , corresponding to the decomposition of acac groups into carbonate,  $\text{CO}_2$  and  $\text{H}_2\text{O}$  [32]. There was no further weight loss after  $300^\circ\text{C}$ , indicating the complete combustion of acac groups and the formation of  $\text{IrO}_x$ . A similar weight loss trend occurred when it comes to  $\text{Ir}(\text{acac})_3/\text{LaFeO}_3$ . In Fig. S1b, the weight loss below  $200^\circ\text{C}$  was attributed to the desorption of  $\text{H}_2\text{O}$  and other impurities absorbed on the surface of the perovskite whereas the decomposition of acac groups occurred from  $200^\circ$  to  $400^\circ\text{C}$ , suggesting that mixing with perovskite had little influence on the decomposition of  $\text{Ir}(\text{acac})_3$ . When the temperature was above  $400^\circ\text{C}$ , negligible weight loss occurred, indicating no organic impurities could be left in the catalysts after calcining  $\text{Ir}(\text{acac})_3/\text{LaFeO}_3$  at the

temperatures we chose ( $300\text{--}600^\circ\text{C}$ ) for 5 h.

The iridium loading was measured by ICP-OES and listed in Table 1. The results for samples calcined at different temperatures were similar, ranging from 0.37 to 0.41 wt%. XRD patterns of the catalysts were presented in Fig. 1a. Typical diffraction peaks of  $\text{LaFeO}_3$  perovskite could be observed (PDF #88-0641) in all catalysts. No diffraction peaks associated with iridium species could be resolved, which could be due to the low loading amount of iridium and/or the high dispersion of Ir on the  $\text{LaFeO}_3$  support. As listed in Table 1, the average crystallite sizes of the  $\text{LaFeO}_3$  support before and after Ir loading calculated by the Scherrer equation showed no significant difference. To further investigate the effect of iridium loading on the support, the most intense peaks of all samples were enlarged and displayed in Fig. 1b. No shifts were observed in the peaks of the perovskite after iridium loading, which ruled out the possibility of iridium doping into the perovskite lattice structure.

FTIR spectra of the iridium catalysts supported on perovskites are displayed in Fig. 1c. The band at  $\sim 538 \text{ cm}^{-1}$  was observed in the spectrum of the support, which was assigned to the Fe–O stretching vibration in the  $\text{FeO}_6$  octahedron [33]. According to Li et al. [34], the stretching vibration of Ir–O bonds was located at  $614 \text{ cm}^{-1}$ . After the iridium loading, neither bands related to iridium nor shifts of Fe–O bands were observed in the spectra, suggesting the probable high dispersion of iridium on the surface of the support, rather than being incorporated into the perovskite structure. To further investigate the state of iridium over the  $\text{LaFeO}_3$  perovskite support, Raman spectra were collected and presented in Fig. 1d. Typical  $\text{LaFeO}_3$  perovskite structure was observed in Raman spectra of all catalysts, consistent with previous literature reports [35–37]. According to Huang et al. [38],  $\text{IrO}_2$  showed two intense Raman active phonon modes, assigned to  $A_{1g}$  ( $\sim 752 \text{ cm}^{-1}$ ) and  $E_g$  ( $\sim 561 \text{ cm}^{-1}$ ). However, neither the Ir–O vibrations in the  $A_{1g}$  and  $E_g$  modes were observed nor new bands were formed in the Raman spectra of all Ir/ $\text{LaFeO}_3$ , indicating that iridium oxide might be highly dispersed on the surface of  $\text{LaFeO}_3$ . Additionally, no shifts in the Raman bands were observed as the calcination temperature increased.

Experiments involving  $\text{N}_2$  adsorption-desorption at 77 K were conducted to examine the textural characteristics of the samples. The results, as depicted in Fig. S2, indicated that all samples exhibited type IV isotherms with hysteresis loops. The specific surface area and the pore volume of  $\text{LaFeO}_3$  support remain unchanged ( $\sim 7 \text{ m}^2 \text{g}^{-1}$  and  $0.03 \text{ cm}^3 \text{g}^{-1}$ ) whether after iridium loading or different temperature calcination, which might be due to the high dispersion of iridium oxide.

As shown in Fig. 2, the morphology and microstructure of iridium catalysts were characterized by TEM. For  $\text{LaFeO}_3$  support (Fig. 2a), aggregated particles and porous structure could be observed, the particle size is around 60 nm. The structure of  $\text{LaFeO}_3$  was further elucidated in HADDF-STEM modes (Fig. 2b). Well-defined cubic  $\text{LaFeO}_3$  perovskite phase could be observed. For iridium-supported catalysts (Fig. 2c, e),

**Table 1**

Chemical composition, average crystallite size, textural properties and hydrogen consumption ( $\text{H}_2 \text{con}$ ) of the catalysts.

Samples	Ir loading <sup>a</sup> (wt%)	La/Fe <sup>a</sup>	$d^b$ (nm)	SSA <sup>c</sup> ( $\text{m}^2 \text{g}^{-1}$ )	$V_p^c$ ( $\text{cm}^3 \text{g}^{-1}$ )	$\text{H}_2 \text{con}^d$ ( $\text{mmol g}^{-1}$ )
$\text{LaFeO}_3$	/	1.0	55.5	7	0.029	0.032
Ir/ $\text{LaFeO}_3$ -300	0.37	1.0	55.2	7	0.030	0.185
Ir/ $\text{LaFeO}_3$ -400	0.38	1.0	55.5	7	0.025	0.160
Ir/ $\text{LaFeO}_3$ -500	0.38	1.0	55.3	7	0.026	0.146
Ir/ $\text{LaFeO}_3$ -600	0.41	1.0	56.8	7	0.026	0.143

<sup>a</sup> calculated by ICP-OES results.

<sup>b</sup> average crystallite size of  $\text{LaFeO}_3$  calculated from XRD diffraction peaks.

<sup>c</sup> specific surface area calculated from  $\text{N}_2$  adsorption-desorption isotherm.

<sup>d</sup>  $\text{H}_2$  consumption amount below  $300^\circ\text{C}$  in  $\text{H}_2$ -TPR experiments.

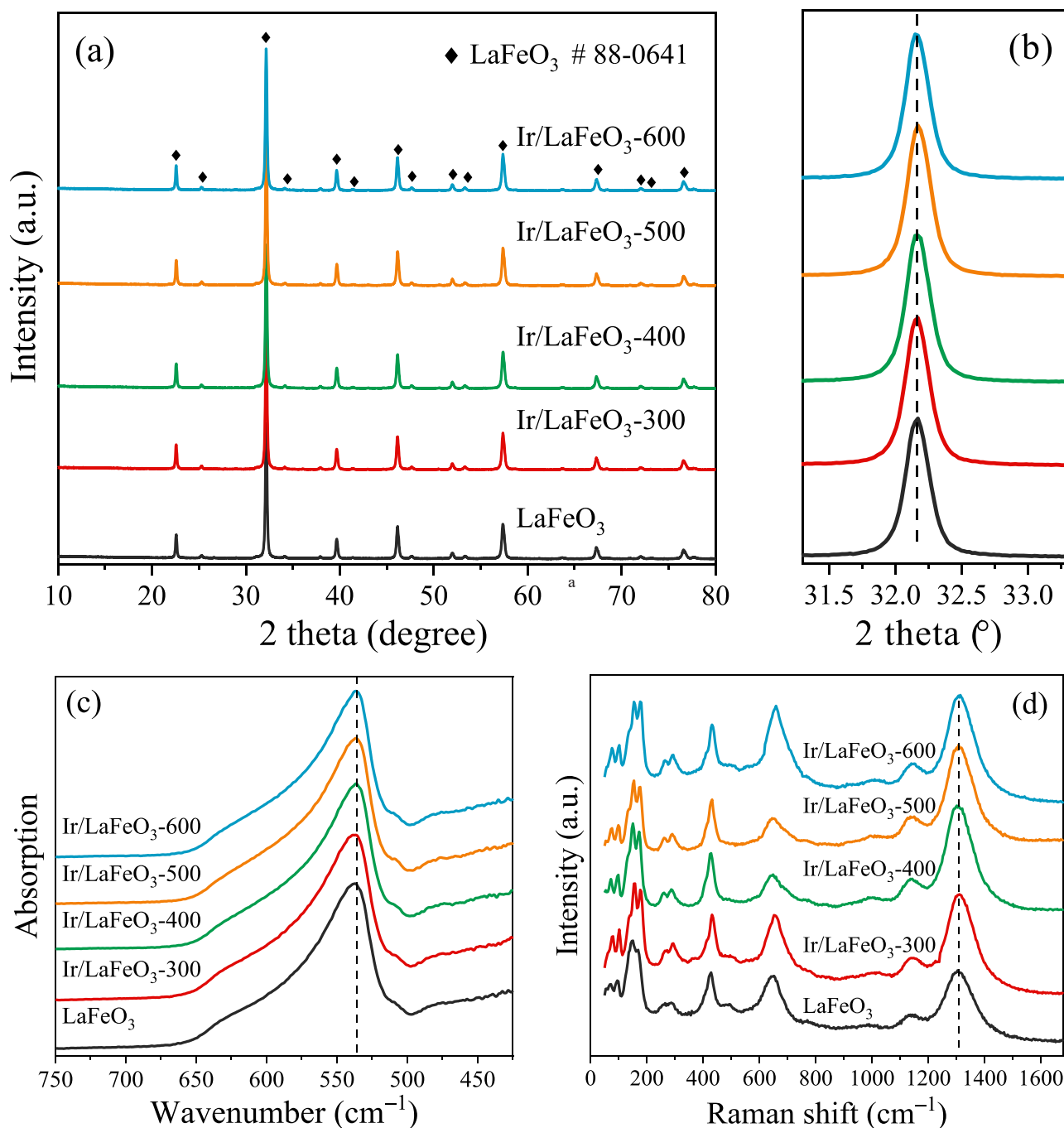


Fig. 1. (a) XRD patterns of the catalysts, (b) comparison of the main XRD peak, (c) FTIR and (d) Raman spectra of the catalysts.

despite the high resolution, no iridium particles or aggregates could be observed in HRTEM images. Fortunately, the presence of iridium has been confirmed by EDX spectroscopy (Fig. 2d, f). In general, the calcination temperature and the nature of the support play a crucial role in determining the dispersion and size of nanoparticles [20]. In our study, no iridium particles were detected even at elevated temperatures. The high dispersion or even atomic dispersion of iridium could be related to the strong interaction between iron and iridium [39].

### 3.2. Redox ability and surface state

Generally, the catalytic oxidation performance is notably influenced by the reducibility of the catalyst at low temperatures [40,41]. Therefore, H<sub>2</sub>-TPR experiments were conducted to study the reducibility of

the iridium catalysts. The profiles were presented in Fig. 3 and the amount of hydrogen consumption was listed in Table 1. For the reduction process of the LaFeO<sub>3</sub> support, two mild peaks at 288 °C and 405 °C were observed, which was attributed to the reduction of adsorbed oxygen species on the surface of LaFeO<sub>3</sub> and the reduction of Fe<sup>4+</sup> to Fe<sup>3+</sup> [42]. As indicated in the literature, the low reducibility of the iron species in the LaFeO<sub>3</sub> structure results in limited reduction peaks in the H<sub>2</sub>-TPR profile [43,44]. After iridium loading, an intense peak at a lower temperature appeared in the profiles of all iridium catalysts, which was assigned to the reduction of iridium species. In addition, the amount of H<sub>2</sub> consumption in the reduction process increased significantly, demonstrating the enhancement in the reducibility of the catalysts by iridium loading. As the calcination temperature increased, the reduction peaks shifted to higher temperatures while the amount of H<sub>2</sub>



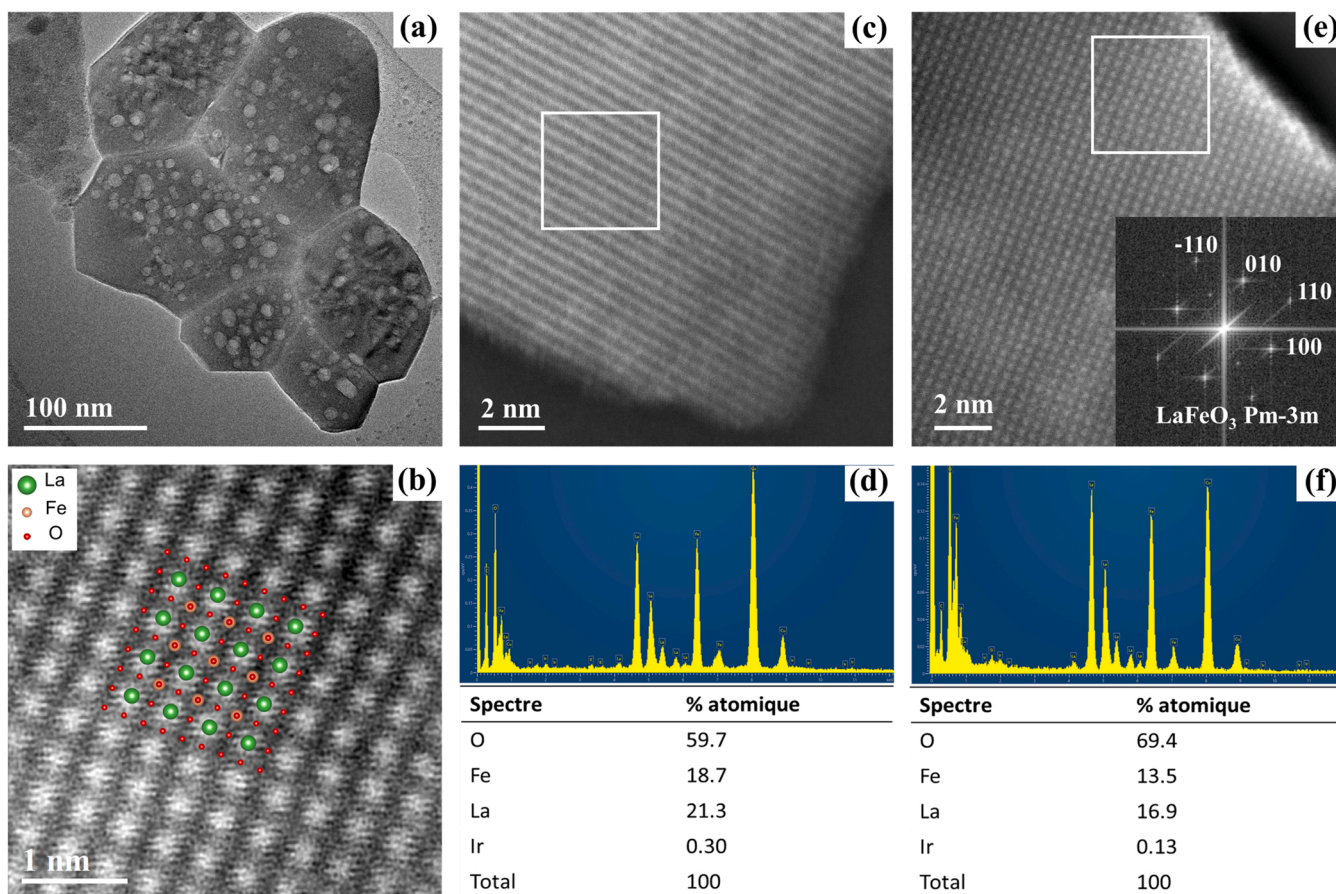


Fig. 2. TEM/HRTEM images and EDX spectra of (a, b)  $\text{LaFeO}_3$  support, (c, d)  $\text{Ir/LaFeO}_3$ -300 and (e, f)  $\text{Ir/LaFeO}_3$ -600.

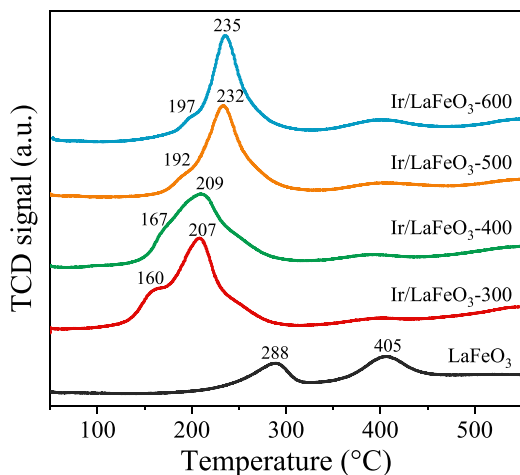


Fig. 3.  $\text{H}_2$ -TPR profiles of the catalysts.

consumption decreased, indicating that high-temperature calcination worsens the reducibility of the iridium catalysts. The  $\text{Ir/LaFeO}_3$ -300 sample showed the largest hydrogen consumption amount and the lowest reduction temperature, making it the catalyst with the best reducibility. Moreover, the small peak observed at 160 °C in  $\text{Ir/LaFeO}_3$ -300 could be attributed to the reduction of adsorbed oxygen species, which could be beneficial to the catalytic oxidation of hydrocarbons.

The surface chemical composition and valence states of the iridium catalysts were analyzed by XPS. La 3d and Fe 2p XPS profiles of typical

catalysts were presented in Fig. S3a, b. For the  $\text{LaFeO}_3$  perovskite support, the peaks at 833.6 eV and 850.3 eV were assigned to La 3d<sub>5/2</sub> and La 3d<sub>3/2</sub> associated with  $\text{La}^{3+}$  while the peaks at 709.8 eV and 723.4 eV were assigned to Fe 2p<sub>3/2</sub> and Fe 2p<sub>1/2</sub> of  $\text{Fe}^{3+}$  in the perovskite [45,46]. After iridium loading, the XPS profiles of La 3d and Fe 2p remained the same without noticeable peak shift, indicating iridium loading had negligible impact on the electronic structure of the  $\text{LaFeO}_3$  support. In Fig. 4a, Ir 4f spectra were deconvoluted into two distinct components and all the samples present similar deconvolution patterns. The first peak located at around 61.4 eV in Ir 4f<sub>7/2</sub> was assigned to  $\text{Ir}^{3+}$  species and the second peak located at around 62.8 eV in Ir 4f<sub>7/2</sub> corresponded to  $\text{Ir}^{4+}$  [20,47]. No bands were detected at approximately 60.8 eV, which is typical of metallic iridium [48,49]. Table 2 listed the calculated ratio of  $\text{Ir}^{3+}$  and  $\text{Ir}^{4+}$  for the catalysts.  $\text{Ir/LaFeO}_3$ -300 exhibited a higher amount of surface  $\text{Ir}^{3+}$  than  $\text{Ir/LaFeO}_3$ -600. The higher concentration of  $\text{Ir}^{3+}$  could contribute to the easier reduction of Ir species, accounting for the better low-temperature reducibility of  $\text{Ir/LaFeO}_3$ -300 revealed by  $\text{H}_2$ -TPR analyses. Additionally, the Ir/La ratio on the surface of the catalysts was significantly higher than that in the bulk, indicating that most of the iridium species were well dispersed on the surface of the  $\text{LaFeO}_3$  support. The O 1s spectra of the catalysts (Fig. 4b) were deconvoluted into three components. The first peak located at ~529 eV was assigned to lattice oxygen, the second peak at ~530.8 eV was assigned to adsorbed oxygen species, and the third peak at ~531.5 eV is due to hydroxyls species and carbonate species [50,51]. As shown in Table 2, the catalyst calcined at 300 °C exhibited the highest concentration of adsorbed oxygen species, indicating the presence of more oxygen vacancies on its surface, which could boost the catalytic performance of propene oxidation.

Propene oxidation without oxygen experiment was conducted to

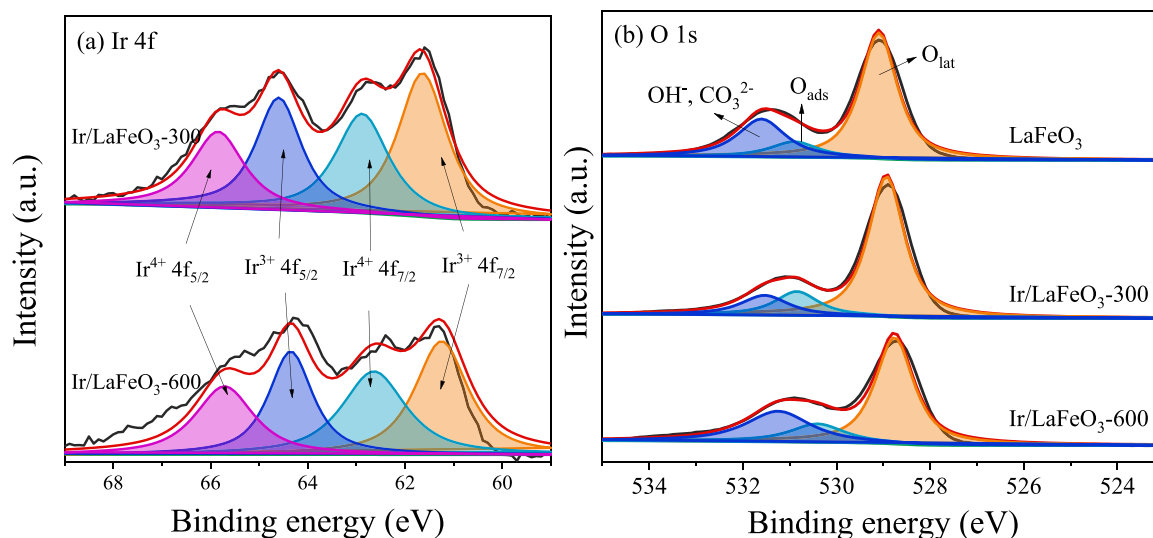


Fig. 4. XPS spectra of the catalysts: (a) Ir 4f and (b) O 1s.

Table 2

XPS results and active oxygen amount of the catalysts.

Samples	Ir <sup>3+</sup> /Ir <sup>4+</sup> <sup>a</sup>	Ir/La surface <sup>a</sup>	Ir/La bulk <sup>b</sup>	O <sub>ads</sub> <sup>a</sup> (%)	active oxygen <sup>c</sup> (μmol g <sup>-1</sup> )
LaFeO <sub>3</sub>	/	/	/	10.3	71.2
Ir/LaFeO <sub>3</sub> -300	1.33	0.037	0.005	14.5	100.6
Ir/LaFeO <sub>3</sub> -600	1.14	0.035	0.005	14.1	75.3

<sup>a</sup> calculated by XPS results.

<sup>b</sup> calculated by ICP-OES results.

<sup>c</sup> calculated by propene oxidation experiment in the absence of gaseous oxygen.

determine the number of active oxygen species on the surface of the catalysts, in which propene was chemisorbed on the surface of the catalyst and oxidized in the absence of oxygen molecular. Fig. 5 depicted the evolution of CO<sub>2</sub> concentration as a function of reaction temperature. Here, the production of CO<sub>2</sub> originates from the complete oxidation of propene. For all catalysts, the production of CO<sub>2</sub> initially increased with rising temperatures, which was attributed to the activation of surface oxygen species. Subsequently, this trend was followed by a decrease due to the gradual consumption of the activated oxygen species. Finally, the active oxygen species on the iridium-supported catalysts could be completely consumed at 450 °C, which failed to be

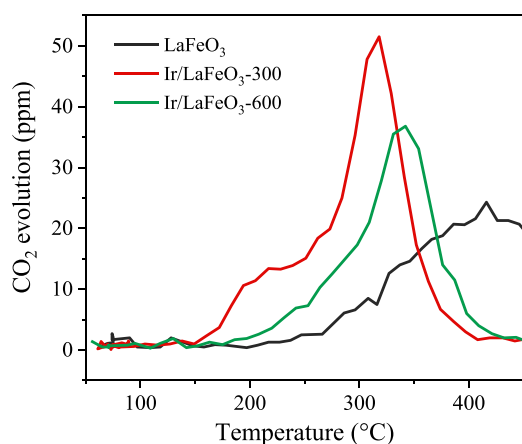


Fig. 5. CO<sub>2</sub> evolution during propene oxidation without O<sub>2</sub>. Test conditions: 1000 ppm C<sub>3</sub>H<sub>6</sub>/He, WHSV = 60000 mL g<sup>-1</sup> h<sup>-1</sup>.

achieved on the LaFeO<sub>3</sub>, suggesting the superior activity of active oxygen species on the iridium catalysts compared to those on the LaFeO<sub>3</sub>. The amount of active oxygen was calculated based on the CO<sub>2</sub> production amount. As shown in Table 2, after iridium loading, the concentration of active oxygen species increased, with Ir/LaFeO<sub>3</sub>-300 exhibiting the highest concentration. The onset temperature of CO<sub>2</sub> production over Ir/LaFeO<sub>3</sub>-300 is around 150 °C, much lower than that over LaFeO<sub>3</sub> (~200 °C), suggesting that the presence of iridium facilitated the activation of oxygen species and enhanced their mobility, thereby promoting propene oxidation. In addition, the lower onset temperature of CO<sub>2</sub> production over Ir/LaFeO<sub>3</sub>-300 compared to Ir/LaFeO<sub>3</sub>-600 (~175 °C) indicated that high-temperature calcination had a negative effect on the oxygen mobility of iridium-supported catalysts.

### 3.3. Catalytic performance

The catalytic performance of the iridium-based catalysts was evaluated using propene as the model VOC. The light-off curves of propene total oxidation over all catalysts were presented in Fig. S4a. In all cases, the only reaction products observed were CO<sub>2</sub> and H<sub>2</sub>O. The CO<sub>2</sub> yield matched well with the propene conversion, indicating an excellent carbon balance. All catalysts reached a full conversion of propene within the tested temperature range, in which LaFeO<sub>3</sub> support exhibited inferior performance. After Ir loading, the catalytic performance of LaFeO<sub>3</sub> was immensely enhanced. All Ir/LaFeO<sub>3</sub> catalysts could achieve 100 % propene conversion below 320 °C. In addition, the light-off curves of Ir/LaFeO<sub>3</sub> catalysts shifted to a higher temperature region with increasing calcination temperature. Among them, Ir/LaFeO<sub>3</sub>-300 exhibited the optimal propene oxidation performance with 50 % conversion at 231 °C and 100 % conversion at 260 °C, which was ~100 °C and ~170 °C lower than that of LaFeO<sub>3</sub>, respectively. To further confirm the performance enhancement provoked by iridium loading, the catalysts were also tested in propane oxidation (Fig. S4b), in which a similar performance enhancement trend was observed.

To better compare the catalytic activity of the Ir/LaFeO<sub>3</sub> catalysts for propene oxidation, the specific reaction rates were calculated taking iridium as the active site. As depicted in Fig. 6, the specific reaction rates decreased as the increase of calcination temperature and Ir/LaFeO<sub>3</sub>-300 showed the highest activity. The reaction rate of LaFeO<sub>3</sub> support was also calculated taking iron as the active site and presented in Fig. S5, which was found to be two orders of magnitude lower than that of Ir/LaFeO<sub>3</sub> catalysts, indicating the substantial increase of the catalytic activity after iridium loading. All the above results indicate that the iridium loading could facilitate the catalytic performance of LaFeO<sub>3</sub> for

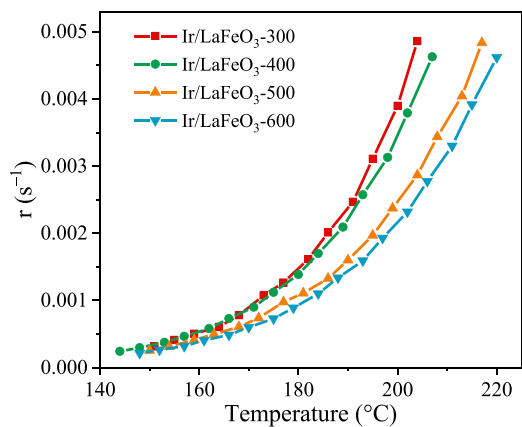


Fig. 6. Specific reaction rates of the iridium-supported catalysts as a function of temperature.

propene oxidation and the calcination temperature had an obvious effect on the catalytic activity of the iridium catalysts. The loading of iridium significantly enhanced the low-temperature reducibility and active oxygen species of the catalyst, which boosted the catalytic activity for total propene oxidation. High-temperature calcination of Ir/LaFeO<sub>3</sub> resulted in worse low-temperature reducibility and less active oxygen species, consequently degrading propene oxidation performance of the catalysts.

Industrial applications place high requirements on the stability and durability of the catalyst. In this study, Ir/LaFeO<sub>3</sub>-300 was chosen as the representative catalyst for the stability test due to its exceptional propene oxidation performance. As shown in Fig. 7a, the durability test was conducted over Ir/LaFeO<sub>3</sub>-300 at 230 °C for 35 h. The propene conversion first experienced a slight decrease over time, and then reached a stable state after around 10 h of reaction at ~40 %. The water resistance of the catalyst is another key issue in practical applications. First, propene oxidation tests over Ir/LaFeO<sub>3</sub>-300, Ir/LaFeO<sub>3</sub>-600, and LaFeO<sub>3</sub> were conducted in dry condition, then 5 vol% of water vapor was introduced into the reaction system, after removing water vapor, a new catalytic cycle was conducted again in dry condition. As presented in Fig. 7b, the catalytic performance of Ir/LaFeO<sub>3</sub>-300 decreased (the T<sub>50</sub>

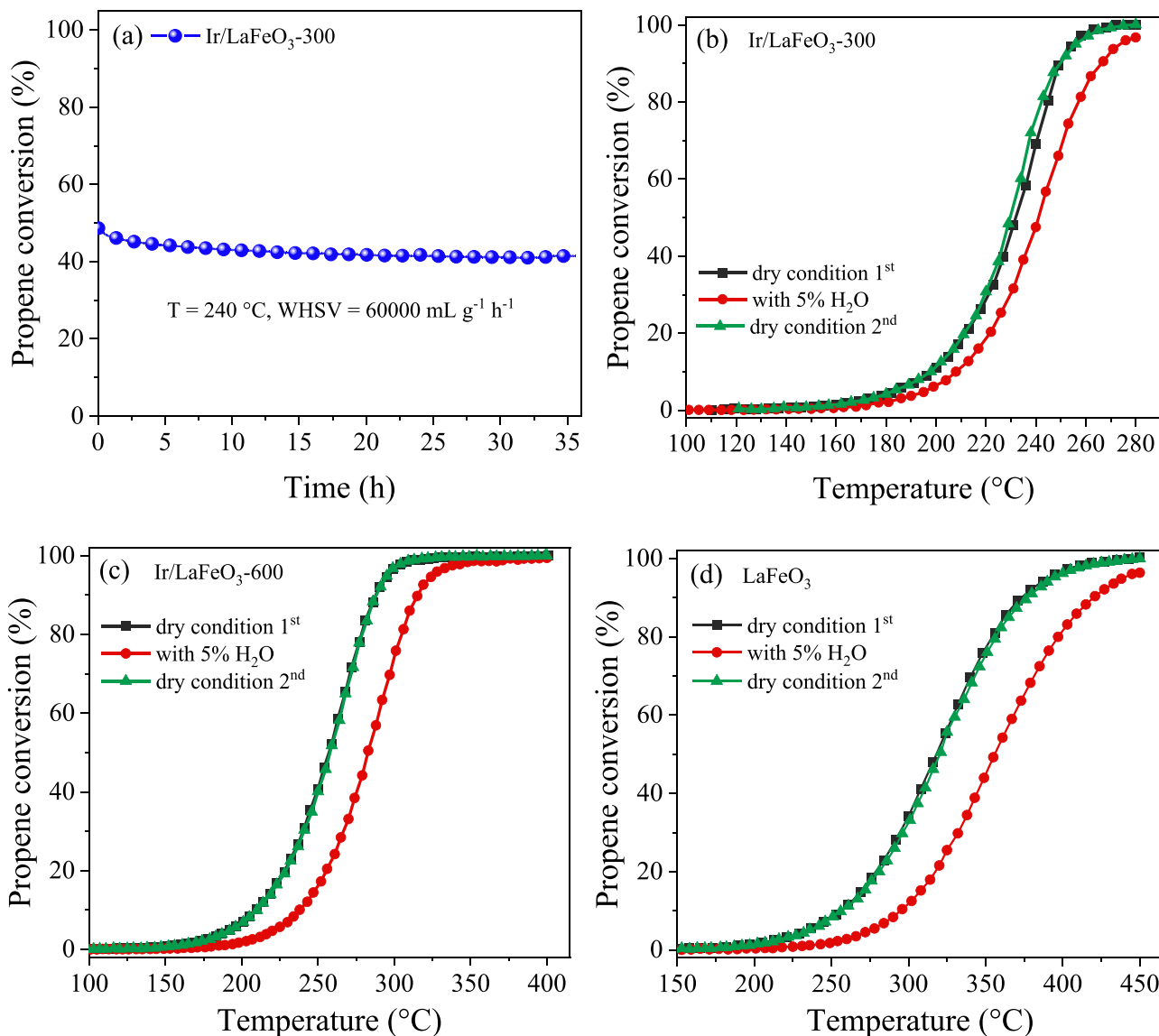


Fig. 7. (a) Stability test for 35 h at 230 °C over Ir/LaFeO<sub>3</sub>-300; effect of 5 vol% water vapor on propene oxidation over (b) Ir/LaFeO<sub>3</sub>-300, (c) Ir/LaFeO<sub>3</sub>-600 and (d) LaFeO<sub>3</sub>. Test condition: 100 mg catalysts + 500 mg SiC, 1000 ppm C<sub>3</sub>H<sub>6</sub> + 21 % O<sub>2</sub>, WHSV = 60000 mL g<sup>-1</sup> h<sup>-1</sup>.

increased by 10 °C) with the introduction of water vapor into the system, which could be attributed to the adsorption of water molecules onto the active sites of the catalyst that impedes the reaction and diminish the catalytic activity [52]. Nevertheless, total oxidation of propene could still be achieved at 280 °C. When water vapor was removed from the feeding gas, the same light-off curve as the original state was reproduced, suggesting that the deactivation caused by water is reversible. Cyclical experiment under water condition was also conducted over Ir/LaFeO<sub>3</sub>-300. As depicted in Fig. S6, no deactivation was observed after a three-cycle test in the presence of water vapor. Fig. 7c and 7d shows that reversible water inhibition effects also occurred on catalysts Ir/LaFeO<sub>3</sub>-600 (the T<sub>50</sub> increased by 20 °C) and LaFeO<sub>3</sub> (the T<sub>50</sub> increased by 36 °C). Notably, Ir/LaFeO<sub>3</sub>-300 exhibited better water resistance than Ir/LaFeO<sub>3</sub>-600 and LaFeO<sub>3</sub>.

Propene and propane were simultaneously introduced into the reaction system to investigate their possible mutual effect during catalytic oxidation over Ir/LaFeO<sub>3</sub>-300 catalyst. Fig. S7 compared the light-off curves of propene and propane oxidation alone or in the mixture. The results indicated that the catalytic conversion of both propene and propane decreased when they were oxidized simultaneously, suggesting the presence of a mutual inhibition effect, which might be due to the competitive adsorption and/or activation of propene and propane over

the active sites of Ir/LaFeO<sub>3</sub>-300. The decrease in propene conversion was much smaller than that in propane conversion, suggesting a stronger interaction between propene and the active sites of Ir/LaFeO<sub>3</sub>-300.

To investigate the effect of support on the catalytic activity of iridium catalysts, iridium catalysts supported on SiO<sub>2</sub>, Al<sub>2</sub>O<sub>3</sub>, and TiO<sub>2</sub> were prepared using the same method as Ir/LaFeO<sub>3</sub> and tested for the total oxidation of propene. As presented in Fig. S8, the specific reaction rates of the iridium catalysts follow the order of Ir/LaFeO<sub>3</sub> > Ir/SiO<sub>2</sub> > Ir/Al<sub>2</sub>O<sub>3</sub> > Ir/TiO<sub>2</sub>. LaFeO<sub>3</sub> was demonstrated to be the best support for iridium catalysts. As discussed above, ultra-high or even atomic dispersion of Ir could be achieved on the LaFeO<sub>3</sub> support due to the strong interaction between Ir and Fe in the support.

Table S1 summarized the catalytic performance of various catalysts for propene oxidation in different testing conditions, including perovskite, metal oxides, and supported noble catalysts. In our study, the catalytic performance of Ir/LaFeO<sub>3</sub>, a catalyst with a relatively small specific surface area, was evaluated under a moderate weight hourly space velocity (WHSV) condition compared to other literature. Despite these suboptimal conditions, Ir/LaFeO<sub>3</sub> exhibited a decent catalytic performance for total propene oxidation when compared to the reported catalysts in the literature. Overall, our findings suggested that Ir/LaFeO<sub>3</sub> could have the potential for practical applications in various industries.

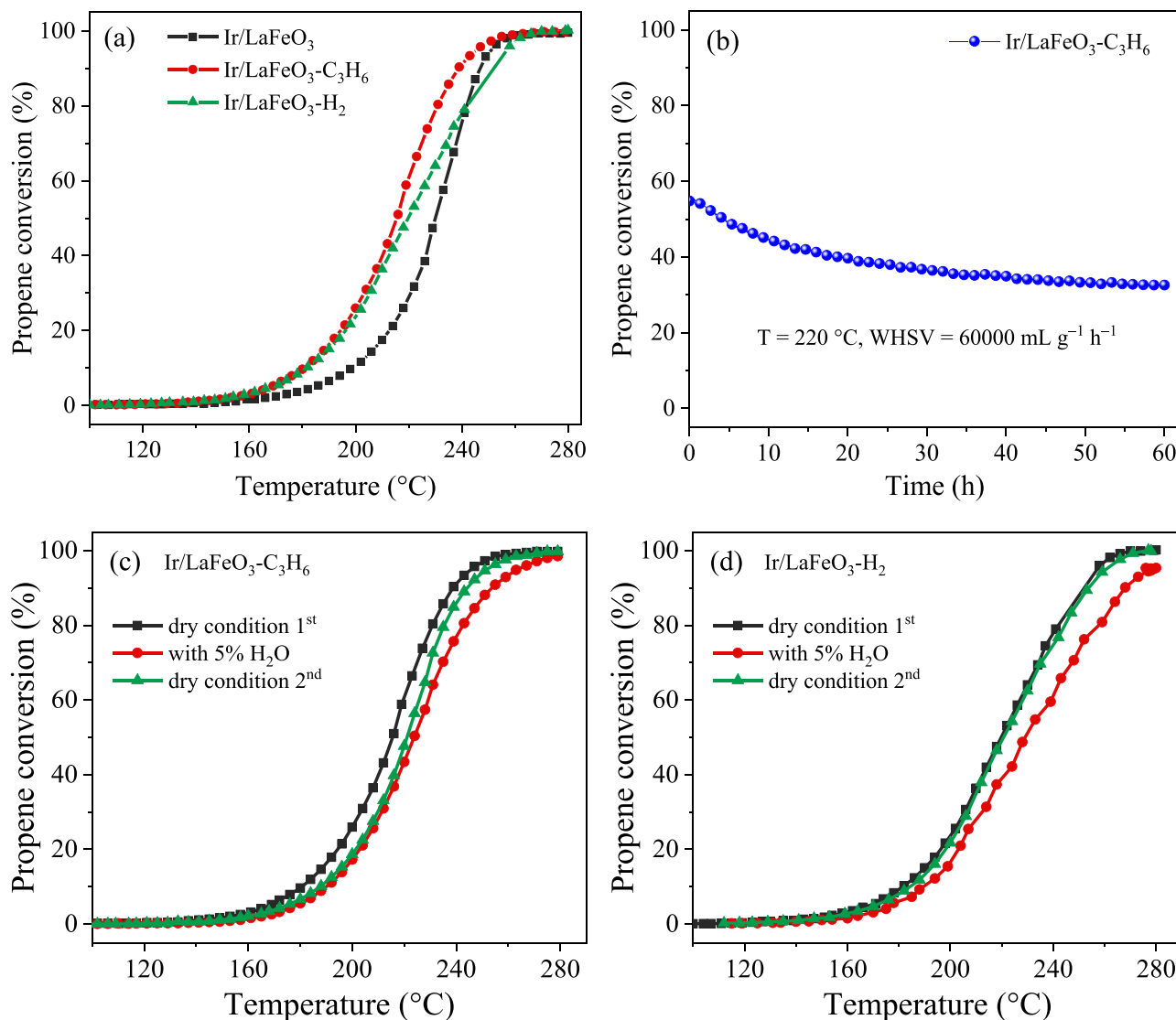


**Fig. 8.** (a) Light-off curves of the as-prepared and reduced catalysts; (b) stability test for 60 h at 220 °C over Ir/LaFeO<sub>3</sub>-C<sub>3</sub>H<sub>6</sub>; effect of 5 vol% water vapor on propene oxidation over (c) Ir/LaFeO<sub>3</sub>-C<sub>3</sub>H<sub>6</sub> and (d) Ir/LaFeO<sub>3</sub>-H<sub>2</sub>. Test condition: 100 mg catalysts + 500 mg SiC, 1000 ppm C<sub>3</sub>H<sub>6</sub> + 21 % O<sub>2</sub>, WHSV = 60000 mL g<sup>-1</sup> h<sup>-1</sup>.



### 3.4. Reduction treatment

Generally, supported noble metal catalysts exhibit higher activity when the noble metals are in a reduction state [8,53]. To illustrate this effect, Ir/LaFeO<sub>3</sub>-300 catalyst was treated by H<sub>2</sub> or C<sub>3</sub>H<sub>6</sub> at 300 °C for 1 h. As shown in Fig. 8a, the catalytic performance of Ir/LaFeO<sub>3</sub>-300 was enhanced after the reduction treatment. Specifically, Ir/LaFeO<sub>3</sub>-C<sub>3</sub>H<sub>6</sub> and Ir/LaFeO<sub>3</sub>-H<sub>2</sub> presented T<sub>50</sub> values of 214 °C and 221 °C, respectively, which was about 17 °C and 10 °C lower than that of Ir/LaFeO<sub>3</sub>-300. In addition, durability and water-resistance tests were conducted on the reduced catalysts. As shown in Fig. 8b, after 60 h of the on-stream test at 220 °C, Ir/LaFeO<sub>3</sub>-C<sub>3</sub>H<sub>6</sub> experienced an obvious decrease in propene conversion (~25 % loss), which suggested the poorer stability of the reduced iridium in propene oxidation than iridium oxide (~7 % loss). Regarding water resistance (Fig. 8c, d), it was observed that the catalytic performance of Ir/LaFeO<sub>3</sub>-C<sub>3</sub>H<sub>6</sub> and Ir/LaFeO<sub>3</sub>-H<sub>2</sub> also slightly decreased in the presence of water vapor, and the extent of decrease was similar to that observed for Ir/LaFeO<sub>3</sub>-300, indicating that iridium catalysts possess decent water resistance whether in oxidized state or in reduced state.

Various characterizations of the reduced catalysts were conducted to reveal the origin of activity enhancement of the iridium catalysts by reduction treatment. As shown in Table S2, the iridium loading remained relatively consistent while the SSA of the Ir/LaFeO<sub>3</sub> increased slightly after the reduction treatment, which might be due to the redistribution of iridium species during the high-temperature reduction process. The low-temperature reducibility of Ir/LaFeO<sub>3</sub> was improved after reduction treatment, as evidenced by the shift of reduction peaks in H<sub>2</sub>-TPR profiles to lower temperatures (Fig. S9a). It is noteworthy that Ir/LaFeO<sub>3</sub>-C<sub>3</sub>H<sub>6</sub> exhibited the highest H<sub>2</sub> consumption, suggesting optimal low-temperature reducibility, which accounted for the better catalytic performance observed in propene oxidation. Fig. S9b depicted the CO<sub>2</sub> evolution during propene oxidation without oxygen and the amount of active oxygen species was calculated in Table S2. It can be observed that the mobility and amount of active oxygen species slightly increased after the reduction treatment. More CO<sub>2</sub> was generated over the reduced catalysts at 150–250 °C than the pristine one, which agrees with their better propene oxidation performance. The surface state of the reduced catalysts was studied by XPS spectra (Fig. 9). In the Ir 4f XPS spectra, the peak at 60.7 eV corresponding to metallic Ir was identified for both Ir/LaFeO<sub>3</sub>-300-H<sub>2</sub> and Ir/LaFeO<sub>3</sub>-C<sub>3</sub>H<sub>6</sub>, indicating the successful reduction of partial cationic Ir to metallic Ir. The peaks at 61.5 eV and 62.4 eV corresponded to Ir<sup>3+</sup> and Ir<sup>4+</sup>, respectively. The surface

contents of Ir<sup>0</sup> and Ir<sup>3+</sup> for the reduced catalysts were calculated and presented in Table S2. Ir/LaFeO<sub>3</sub>-C<sub>3</sub>H<sub>6</sub> exhibited a lower reduction degree compared to Ir/LaFeO<sub>3</sub>-H<sub>2</sub>, as evidenced by a lower proportion of Ir<sup>0</sup> and a higher proportion of Ir<sup>3+</sup>. It was reported that the presence of Ir<sup>3+</sup> could be associated with the presence of oxygen vacancies on the surface of the IrO<sub>x</sub> [54,55]. Accordingly, the higher proportion of Ir<sup>3+</sup> observed in Ir/LaFeO<sub>3</sub>-C<sub>3</sub>H<sub>6</sub> implied a greater concentration of oxygen vacancies on its surface, which could contribute to better propene oxidation performance [56,57]. In Fig. 9b, the O 1s spectra were deconvoluted into three components, among which the peak at 530.9 eV was assigned to absorbed oxygen species. As summarized in Table S2, Ir/LaFeO<sub>3</sub>-C<sub>3</sub>H<sub>6</sub> exhibited the largest amount of absorbed oxygen species, which agrees well with the presence of abundant oxygen vacancies in the IrO<sub>x</sub>, leading to superior propene oxidation performance. Summarizing up, the low-temperature reducibility and active oxygen mobility of the iridium catalysts were improved after reduction treatment, which was responsible for their enhanced catalytic performance in total propene oxidation.

### 4. Conclusion

In the work, a facile solvent-free strategy was developed for the preparation of highly dispersed iridium catalysts supported on LaFeO<sub>3</sub>. The characterization results showed that iridium was well dispersed on LaFeO<sub>3</sub> without any detectable particles or aggregates. Ir loading hardly changed the specific surface area and structure of LaFeO<sub>3</sub>, whereas greatly enhanced the reducibility. The propene oxidation performance of LaFeO<sub>3</sub> was significantly promoted by Ir. The catalytic activity of Ir/LaFeO<sub>3</sub> decreases with the calcination temperature, which correlates well with the low-temperature reducibility of the catalysts. The optimal catalyst, Ir/LaFeO<sub>3</sub>-300, showed not only the best performance (T<sub>50</sub> = 231 °C, T<sub>100</sub> = 260 °C) but also good long-term durability and decent water resistance. Moreover, the catalytic performance of Ir/LaFeO<sub>3</sub>-300 could be further improved via H<sub>2</sub> or C<sub>3</sub>H<sub>6</sub> reduction treatment, which was attributed to the enhanced low-temperature reducibility and increase in the number of surface-active oxygen species.

### CRediT authorship contribution statement

This work was done jointly by all authors. Feng Pan prepared the catalysts, performed structural characterizations and catalytic oxidation tests, and wrote the first draft of the manuscript. Weidong Zhang helped do catalyst preparations and experiments. Weidong Zhang, Corinne

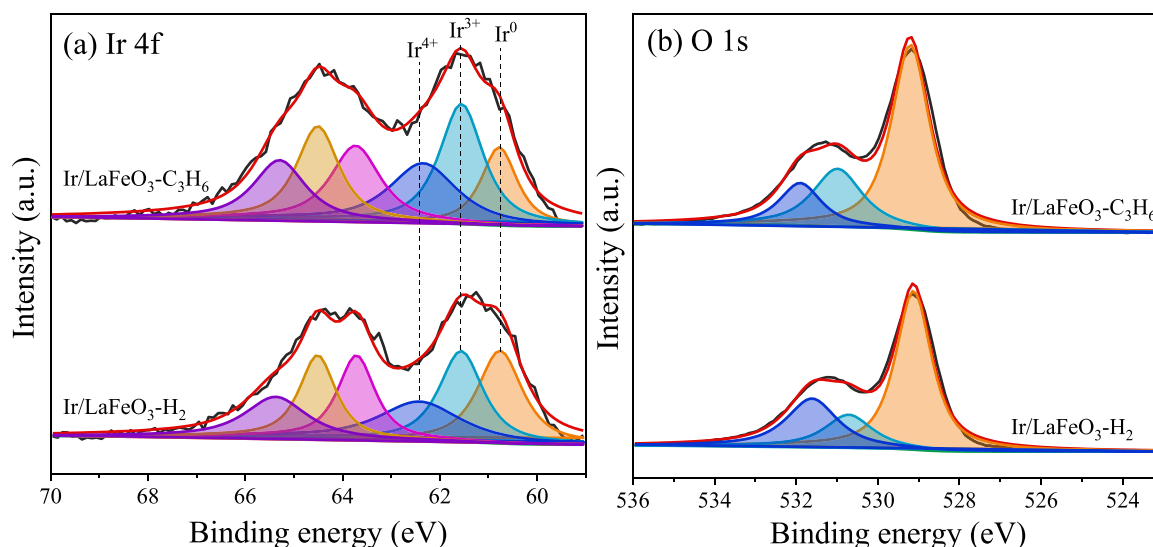


Fig. 9. XPS spectra for the reduced iridium catalysts: (a) Ir 4f and (b) O 1s.

Ferronato and Jose Luis Valverde participated for data interpretation, result discussion, and manuscript review and revision. Anne Giroir-Fendler coordinated the whole study, e.g., funding acquisition, resources, validation, supervision, project administration, review & editing.

### Declaration of Competing Interest

The authors declare that they have no known competing financial interests or personal relationships that could have appeared to influence the work reported in this paper.

### Data availability

No data was used for the research described in the article.

### Acknowledgements

This work was financially supported by the Université Claude Bernard Lyon 1 and CNRS. We gratefully acknowledge the China Scholarship Council of P.R. China for Feng PAN's grant.

### Appendix A. Supporting information

Supplementary data associated with this article can be found in the online version at [doi:10.1016/j.apcatb.2023.123406](https://doi.org/10.1016/j.apcatb.2023.123406).

### References

- W. Zhang, K. Lassen, C. Descorme, J.L. Valverde, A. Giroir-Fendler, Effect of the precipitation pH on the characteristics and performance of  $\text{Co}_3\text{O}_4$  catalysts in the total oxidation of toluene and propane, *Appl. Catal. B Environ.* 282 (2021), 119566, <https://doi.org/10.1016/j.apcatb.2020.119566>.
- N. Mohd Hanif, N.S.S. Limi Hawari, M. Othman, H.H. Abd Hamid, F. Ahmad, R. Uning, M.C.G. Ooi, M.I.A. Wahab, M. Sahani, M.T. Latif, Ambient volatile organic compounds in tropical environments: potential sources, composition and impacts – a review, *Chemosphere* 285 (2021), 131355, <https://doi.org/10.1016/j.chemosphere.2021.131355>.
- C. Yang, G. Miao, Y. Pi, Q. Xia, J. Wu, Z. Li, J. Xiao, Abatement of various types of VOCs by adsorption/catalytic oxidation: a review, *Chem. Eng. J.* 370 (2019) 1128–1153, <https://doi.org/10.1016/j.cej.2019.03.232>.
- Y. Fang, L. Li, J. Yang, S. Hoang, L. Wang, J. Xu, W. Yang, C. Pan, Y. Zhu, H. Deng, Z. Luo, C. Sun, D. Gao, Z. Li, Y. Guo, Engineering the nucleophilic active oxygen species in  $\text{CuTiO}_x$  for efficient low-temperature propene combustion, *Environ. Sci. Technol.* 54 (2020) 15476–15488, <https://doi.org/10.1021/acs.est.0c05845>.
- M.S. Kamal, S.A. Razzak, M.M. Hossain, Catalytic oxidation of volatile organic compounds (VOCs) - a review, *Atmos. Environ.* 140 (2016) 117–134, <https://doi.org/10.1016/j.atmosenv.2016.05.031>.
- Y. Guo, M. Wen, G. Li, T. An, Recent advances in VOC elimination by catalytic oxidation technology onto various nanoparticles catalysts: a critical review, *Appl. Catal. B Environ.* 281 (2021), 119447, <https://doi.org/10.1016/j.apcatb.2020.119447>.
- S. Gil, J.M. Garcia-Vargas, L.F. Liotta, G. Pantaleo, M. Ousmane, L. Retailleau, A. Giroir-Fendler, Catalytic oxidation of propene over Pd catalysts supported on  $\text{CeO}_2$ ,  $\text{TiO}_2$ ,  $\text{Al}_2\text{O}_3$  and  $\text{M}/\text{Al}_2\text{O}_3$  oxides ( $\text{M} = \text{Ce}, \text{Ti}, \text{Fe}, \text{Mn}$ ), *Catalysts* 5 (2015) 671–689, <https://doi.org/10.3390/catal5020671>.
- H. Huang, Y. Xu, Q. Feng, D.Y.C. Leung, Low temperature catalytic oxidation of volatile organic compounds: a review, *Catal. Sci. Technol.* 5 (2015) 2649–2669, <https://doi.org/10.1039/C4CY01733A>.
- H.S. Kim, H.J. Kim, J.H. Kim, J.H. Kim, S.H. Kang, J.H. Ryu, N.K. Park, D.S. Yun, J. W. Bae, Noble-metal-based catalytic oxidation technology trends for volatile organic compound (VOC) removal, *Catalysts* 12 (2022), <https://doi.org/10.3390/catal12010063>.
- P. Yang, J. Li, Z. Cheng, S. Zuo, Promoting effects of Ce and Pt addition on the destructive performances of  $\text{V}_2\text{O}_5/\text{T}-\text{Al}_2\text{O}_3$  for catalytic combustion of benzene, *Appl. Catal. A Gen.* 542 (2017) 38–46, <https://doi.org/10.1016/j.apcata.2017.05.016>.
- Y. Fang, H. Li, Q. Zhang, C. Wang, J. Xu, H. Shen, J. Yang, C. Pan, Y. Zhu, Z. Luo, Y. Guo, Oxygen vacancy-governed opposite catalytic performance for  $\text{C}_3\text{H}_6$  and  $\text{C}_3\text{H}_8$  combustion: the effect of the Pt electronic structure and chemisorbed oxygen species, *Environ. Sci. Technol.* (2022), <https://doi.org/10.1021/acs.est.1c07573>.
- J. Yan, L. Wang, Y. Guo, Y. Guo, Q. Dai, W. Zhan, Comparisons on thermal and water-resistance of Ru and Pd supported on cobalt-doped alumina nanosheets for catalytic combustion of propane, *Appl. Catal. A Gen.* 628 (2021), 118398, <https://doi.org/10.1016/j.apcata.2021.118398>.
- W. Yang, X. Zhang, J. Su, Y. Wang, Q. Zhao, J. Zhou, Kinetics of n-butanol oxidation over Pt/ZSM-5 catalyst, *Fuel Process. Technol.* 179 (2018) 108–113, <https://doi.org/10.1016/j.fuproc.2018.06.020>.
- H.J. Joung, J.H. Kim, J.S. Oh, D.W. You, H.O. Park, K.W. Jung, Catalytic oxidation of VOCs over CNT-supported platinum nanoparticles, *Appl. Surf. Sci.* 290 (2014) 267–273, <https://doi.org/10.1016/j.apsusc.2013.11.066>.
- N. Tahsini, A.C. Yang, V. Streibel, B. Werghi, E.D. Goodman, A. Aitbekova, S. R. Bare, Y. Li, F. Abild-Pedersen, M. Cargnello, Colloidal platinum-copper nanocrystal alloy catalysts surpass platinum in low-temperature propene combustion, *J. Am. Chem. Soc.* 144 (2022) 1612–1621, <https://doi.org/10.1021/jacs.1c10248>.
- Z. Wang, P. Ma, K. Zheng, C. Wang, Y. Liu, H. Dai, C. Wang, H.-C. Hsi, J. Deng, Size effect, mutual inhibition and oxidation mechanism of the catalytic removal of a toluene and acetone mixture over  $\text{TiO}_2$  nanosheet-supported Pt nanocatalysts, *Appl. Catal. B Environ.* 274 (2020), 118963, <https://doi.org/10.1016/j.apcatb.2020.118963>.
- H. Tanaka, M. Uenishi, M. Taniguchi, I. Tan, K. Narita, M. Kimura, K. Kaneko, Y. Nishihata, J. Mizuki, The intelligent catalyst having the self-regenerative function of Pd, Rh and Pt for automotive emissions control, *Catal. Today* 117 (2006) 321–328, <https://doi.org/10.1016/j.cattod.2006.05.029>.
- S. Hyok Ri, F. Bi, A. Guan, X. Zhang, Manganese-cerium composite oxide pyrolyzed from metal organic framework supporting palladium nanoparticles for efficient toluene oxidation, *J. Colloid Interface Sci.* 586 (2021) 836–846, <https://doi.org/10.1016/j.jcis.2020.11.008>.
- L. Schick, R. Sanchis, V. González-Alfaro, S. Agouram, J.M. López, L. Torrente-Murciano, T. García, B. Solsona, Size-activity relationship of iridium particles supported on silica for the total oxidation of volatile organic compounds (VOCs), *Chem. Eng. J.* 366 (2019) 100–111, <https://doi.org/10.1016/j.cej.2019.02.087>.
- L. Schick, V. González-Alfaro, A. García, J.M. López, D.J. Morgan, S. Agouram, S. H. Taylor, T. García, B. Solsona, Supported iridium catalysts for the total oxidation of short chain alkanes and their mixtures: influence of the support, *Chem. Eng. J.* (2020), <https://doi.org/10.1016/j.cej.2020.127999>.
- X. Sun, J. Lin, Y. Wang, L. Li, X. Pan, Y. Su, X. Wang, Catalytically active IrO<sub>2</sub> species supported on  $\text{Al}_2\text{O}_3$  for complete oxidation of formaldehyde at ambient temperature, *Appl. Catal. B Environ.* 268 (2020), 118741, <https://doi.org/10.1016/j.apcatb.2020.118741>.
- Y. Li, X. Chen, C. Wang, C. Zhang, H. He, Sodium enhances Ir/TiO<sub>2</sub> activity for catalytic oxidation of formaldehyde at ambient temperature, *ACS Catal.* 8 (2018) 11377–11385, <https://doi.org/10.1021/acscatal.8b03026>.
- F. Bi, X. Zhang, J. Chen, Y. Yang, Y. Wang, Excellent catalytic activity and water resistance of UiO-66-supported highly dispersed Pd nanoparticles for toluene catalytic oxidation, *Appl. Catal. B Environ.* 269 (2020), 118767, <https://doi.org/10.1016/j.apcatb.2020.118767>.
- L. Wang, M.X. Chen, Q.Q. Yan, S.L. Xu, S.Q. Chu, P. Chen, Y. Lin, H.W. Liang, A sulfur-tethering synthesis strategy toward high-loading atomically dispersed noble metal catalysts, *Sci. Adv.* 5 (2019), <https://doi.org/10.1126/sciadv.aax6322>.
- D. Chen, J. Shi, H. Shen, High-dispersed catalysts of core-shell structured Au@SiO<sub>2</sub> for formaldehyde catalytic oxidation, *Chem. Eng. J.* 385 (2020), 123887, <https://doi.org/10.1016/j.cej.2019.123887>.
- F. Gu, Y. Cui, D. Han, S. Hong, M. Flytzani-Stephanopoulos, Z. Wang, Atomically dispersed Pt(II) on WO<sub>3</sub> for highly selective sensing and catalytic oxidation of triethylamine, *Appl. Catal. B Environ.* 256 (2019), 117809, <https://doi.org/10.1016/j.apcatb.2019.117809>.
- Z. Chen, J. Mao, R. Zhou, Preparation of size-controlled Pt supported on  $\text{Al}_2\text{O}_3$  nanocatalysts for deep catalytic oxidation of benzene at lower temperature, *Appl. Surf. Sci.* 465 (2019) 15–22, <https://doi.org/10.1016/j.apsusc.2018.09.138>.
- S. Liu, N. Tang, Q. Shang, C. Wu, G. Xu, Y. Cong, Superior performance of iridium supported on rutile titania for the catalytic decomposition of N<sub>2</sub>O propellants, *Cuihua Xuebao/Chin. J. Catal.* 39 (2018) 1189–1193, [https://doi.org/10.1016/S1872-2067\(18\)63077-3](https://doi.org/10.1016/S1872-2067(18)63077-3).
- K. Liu, X. Zhao, G. Ren, T. Yang, Y. Ren, A.F. Lee, Y. Su, X. Pan, J. Zhang, Z. Chen, J. Yang, X. Liu, T. Zhou, W. Xi, J. Luo, C. Zeng, H. Matsumoto, W. Liu, Q. Jiang, K. Wilson, A. Wang, B. Qiao, W. Li, T. Zhang, Strong metal-support interaction promoted scalable production of thermally stable single-atom catalysts, *Nat. Commun.* 11 (1) (2020) 9, <https://doi.org/10.1038/s41467-020-14984-9>.
- S.P. Joshi, T.T. Pekkanen, R.S. Timonen, G. Lendvay, A.J. Eskola, Kinetics of the methyl-vinyl radical + O<sub>2</sub> reactions associated with propene oxidation, *J. Phys. Chem. A* 123 (2019) 999–1006, <https://doi.org/10.1021/acs.jpca.8b11017>.
- Z. Zhang, D. Han, S. Wei, Y. Zhang, Determination of active site densities and mechanisms for soot combustion with O<sub>2</sub> on Fe-doped  $\text{CeO}_2$  mixed oxides, *J. Catal.* 276 (2010) 16–23, <https://doi.org/10.1016/j.jcat.2010.08.017>.
- S. Nassreddine, G. Bergeret, B. Jouguet, C. Geantet, L. Piccolo, Operando study of iridium acetylacetonate decomposition on amorphous silica-alumina for bifunctional catalyst preparation, *Phys. Chem. Chem. Phys.* 12 (2010) 7812–7820, <https://doi.org/10.1039/b925062j>.
- K.H. Saeed, M. Forster, J.F. Li, L.J. Hardwick, A.J. Cowan, Water oxidation intermediates on iridium oxide electrodes probed by: In situ electrochemical SHINERS, *Chem. Commun.* 56 (2020) 1129–1132, <https://doi.org/10.1039/c9cc08284k>.
- L. Li, G. Li, Y. Zhang, W. Ouyang, H. Zhang, F. Dong, X. Gao, Z. Lin, Fabricating nano-IrO<sub>2</sub>@amorphous Ir-MOF composites for efficient overall water splitting: a one-pot solvothermal approach, *J. Mater. Chem. A* 8 (2020) 25687–25695, <https://doi.org/10.1039/d0ta09168e>.
- F. Pan, T. Chen, M. Cai, F. Wu, Z. You, J. Li, Fabrication of large-surface-area graphitized carbons by potassium hydroxide-promoted catalytic graphitization,

- Mater. Res. Bull. 140 (2021), 111333, <https://doi.org/10.1016/j.materresbull.2021.111333>.
- [36] T. Bhowmick, S. Nag, S.B. Majumder, Investigations on lanthanum iron cobalt oxide thin film as selective carbon monoxide sensor, *J. Alloy. Compd.* 884 (2021), 161161, <https://doi.org/10.1016/j.jallcom.2021.161161>.
- [37] J. Ma, Z. Geng, Y. Jiang, X. Hou, X. Ge, Z. Wang, K. Huang, W. Zhang, S. Feng, Exsolution manipulated local surface cobalt/iron alloying and dealloying conversion in  $\text{La}_{0.95}\text{Fe}_{0.8}\text{Co}_{0.2}\text{O}_3$  perovskite for oxygen evolution reaction, *J. Alloy. Compd.* 854 (2021), 157154, <https://doi.org/10.1016/j.jallcom.2020.157154>.
- [38] Y.S. Huang, S.S. Lin, C.R. Huang, M.C. Lee, T.E. Dann, F.Z. Chien, Raman spectrum of  $\text{IrO}_2$ , *Solid State Commun.* 70 (1989) 517–522, [https://doi.org/10.1016/0038-1098\(89\)90942-3](https://doi.org/10.1016/0038-1098(89)90942-3).
- [39] B. Liu, Y. Nakagawa, C. Li, M. Yabushita, K. Tomishige, Selective C–O Hydrogenolysis of terminal C–OH bond in 1,2-Diols over rutile-titania-supported iridium-iron catalysts, *ACS Catal.* (2022) 15431–15450, <https://doi.org/10.1021/acscatal.2c04499>.
- [40] C. Zhang, Y. Guo, Y. Guo, G. Lu, A. Boreave, L. Retaillieu, A. Baylet, A. Giroir-Fendler,  $\text{LaMnO}_3$  perovskite oxides prepared by different methods for catalytic oxidation of toluene, *Appl. Catal. B Environ.* 148–149 (2014) 490–498, <https://doi.org/10.1016/j.apcatb.2013.11.030>.
- [41] F. Zhang, X. Zhang, G. Jiang, N. Li, Z. Hao, S. Qu,  $\text{H}_2\text{S}$  selective catalytic oxidation over Ce substituted  $\text{La}_{1-x}\text{Ce}_x\text{FeO}_3$  perovskite oxides catalyst, *Chem. Eng. J.* 348 (2018) 831–839, <https://doi.org/10.1016/j.cej.2018.05.050>.
- [42] S. Zhao, L. Wang, Y. Wang, X. Li, Hierarchically porous  $\text{LaFeO}_3$  perovskite prepared from the pomelo peel bio-template for catalytic oxidation of NO, *J. Phys. Chem. Solids* 116 (2018) 43–49, <https://doi.org/10.1016/j.jpcs.2017.12.057>.
- [43] K.T.C. Roseno, R. Brackmann, M.A. da Silva, M. Schmal, Investigation of  $\text{LaCoO}_3$ ,  $\text{LaFeO}_3$  and  $\text{LaCo}_{0.5}\text{Fe}_{0.5}\text{O}_3$  perovskites as catalyst precursors for syngas production by partial oxidation of methane, *Int. J. Hydrog. Energy* 41 (2016) 18178–18192, <https://doi.org/10.1016/j.ijhydene.2016.07.207>.
- [44] M. Dreyer, M. Krebs, S. Najafshirvani, A. Rabe, K.F. Ortega, M. Behrens, The effect of Co incorporation on the CO oxidation activity of  $\text{LaFe}_{1-x}\text{Co}_x\text{O}_3$  perovskites, *Catalysts* 11 (2021), <https://doi.org/10.3390/catal11050550>.
- [45] P. Hao, P. Song, Z. Yang, Q. Wang, Synthesis of novel  $\text{RuO}_2/\text{LaFeO}_3$  porous microspheres its gas sensing performances towards triethylamine, *J. Alloy. Compd.* 806 (2019) 960–967, <https://doi.org/10.1016/j.jallcom.2019.07.313>.
- [46] J.M. Giraudon, A. Elhachimi, F. Wyrwalski, S. Siffert, A. Aboukais, J.F. Lamonier, G. Leclercq, Studies of the activation process over Pd perovskite-type oxides used for catalytic oxidation of toluene, *Appl. Catal. B Environ.* 75 (2007) 157–166, <https://doi.org/10.1016/j.apcatb.2007.04.005>.
- [47] S. Li, Y. Xu, Y. Chen, W. Li, L. Lin, M. Li, Y. Deng, X. Wang, B. Ge, C. Yang, S. Yao, J. Xie, Y. Li, X. Liu, D. Ma, Tuning the selectivity of catalytic carbon dioxide hydrogenation over iridium/cerium oxide catalysts with a strong metal-support interaction, *Angew. Chem.* 129 (2017) 10901–10905, <https://doi.org/10.1002/ange.201705002>.
- [48] N.S. Date, A.M. Hengne, K.W. Huang, R.C. Chikate, C.V. Rode, Single pot selective hydrogenation of furfural to 2-methylfuran over carbon supported iridium catalysts, *Green. Chem.* 20 (2018) 2027–2037, <https://doi.org/10.1039/c8gc00284c>.
- [49] V. Pfeifer, T.E. Jones, J.J. Velasco Vélez, C. Massué, R. Arrigo, D. Teschner, F. Girgsdies, M. Scherzer, M.T. Greiner, J. Allan, M. Hashagen, G. Weinberg, S. Piccinin, M. Hävecker, A. Knop-Gericke, R. Schlögl, The electronic structure of iridium and its oxides, *Surf. Interface Anal.* 48 (2016) 261–273, <https://doi.org/10.1002/sia.5895>.
- [50] M. Wu, S. Chen, W. Xiang, Oxygen vacancy induced performance enhancement of toluene catalytic oxidation using  $\text{LaFeO}_3$  perovskite oxides, *Chem. Eng. J.* 387 (2020), 124101, <https://doi.org/10.1016/j.cej.2020.124101>.
- [51] J. Zhang, D. Tan, Q. Meng, X. Weng, Z. Wu, Structural modification of  $\text{LaCoO}_3$  perovskite for oxidation reactions: the synergistic effect of  $\text{Ca}^{2+}$  and  $\text{Mg}^{2+}$  co-substitution on phase formation and catalytic performance, *Appl. Catal. B Environ.* 172–173 (2015) 18–26, <https://doi.org/10.1016/j.apcatb.2015.02.006>.
- [52] G. Chai, W. Zhang, L.F. Liotta, M. Li, Y. Guo, A. Giroir-Fendler, Total oxidation of propane over  $\text{Co}_3\text{O}_4$ -based catalysts: elucidating the influence of Zr dopant, *Appl. Catal. B Environ.* 298 (2021), 120606, <https://doi.org/10.1016/j.apcatb.2021.120606>.
- [53] T. Lan, Y. Zhao, J. Deng, J. Zhang, L. Shi, D. Zhang, Selective catalytic oxidation of  $\text{NH}_3$  over noble metal-based catalysts: state of the art and future prospects, *Catal. Sci. Technol.* 10 (2020) 5792–5810, <https://doi.org/10.1039/d0cy01137a>.
- [54] S.H. Cho, K.R. Yoon, K. Shin, J.W. Jung, C. Kim, J.Y. Cheong, D.Y. Youn, S. W. Song, G. Henkelman, I.D. Kim, Synergistic coupling of metallic cobalt nitride nanofibers and  $\text{IrO}_x$  nanoparticle catalysts for stable oxygen evolution, *Chem. Mater.* 30 (2018) 5941–5950, <https://doi.org/10.1021/acs.chemmater.8b02061>.
- [55] Z. Xiao, Y.C. Huang, C.L. Dong, C. Xie, Z. Liu, S. Du, W. Chen, D. Yan, L. Tao, Z. Shu, G. Zhang, H. Duan, Y. Wang, Y. Zou, R. Chen, S. Wang, Operando identification of the dynamic behavior of oxygen vacancy-rich  $\text{Co}_3\text{O}_4$  for oxygen evolution reaction, *J. Am. Chem. Soc.* 142 (2020) 12087–12095, <https://doi.org/10.1021/jacs.0c00257>.
- [56] J. Yang, S. Hu, L. Shi, S. Hoang, W. Yang, Y. Fang, Z. Liang, C. Pan, Y. Zhu, L. Li, J. Wu, J. Hu, Y. Guo, Oxygen vacancies and lewis acid sites synergistically promoted catalytic methane combustion over perovskite oxides, *Environ. Sci. Technol.* (2021), <https://doi.org/10.1021/acs.est.1c00511>.
- [57] Y. Zheng, Y. Su, C. Pang, L. Yang, C. Song, N. Ji, D. Ma, X. Lu, R. Han, Q. Liu, Interface-enhanced oxygen vacancies of  $\text{CoCuO}_x$  catalysts in situ grown on monolithic Cu foam for VOC catalytic oxidation, *Environ. Sci. Technol.* 56 (2022) 1905–1916, <https://doi.org/10.1021/acs.est.1c05855>.